AIAA 2001–2414

DRAG PREDICTION OF ENGINE–AIRFRAME INTERFERENCE EFFECTS USING UNSTRUCTURED NAVIER–STOKES CALCULATIONS

O. Brodersen, A. Stürmer
DLR Institute of Design Aerodynamics,
Braunschweig, Germany

19th AIAA Applied Aerodynamics Conference
11-14 June 2001
Anaheim, California

DRAG PREDICTION OF ENGINE–AIRFRAME INTERFERENCE EFFECTS USING UNSTRUCTURED NAVIER–STOKES CALCULATIONS

O. Brodersen, * A. Stürmer †
DLR Institute of Design Aerodynamics, Braunschweig, Germany

Abstract

Navier–Stokes calculations on hybrid grids are performed to compute engine installation drag for the DLR–F6 aircraft configuration with conventional and with Very–High–Bypass–Ratio nacelles at three and two different locations, respectively. The results are verified by a comparison with experimental data from wind tunnel campaigns. Numerical discretization errors are reduced by several steps of grid adaptation resulting in grid densities up to 8.4 million nodes. It is demonstrated that the installation drag of the different configurations, which vary only a few drag counts (10^{-4}), can be computed consistently, although the total drag forces are predicted lower than in the experiments. Grid refinement leads to a decrease of the differences between calculated and measured installation drag.

Introduction

One key aspect during the design of an enhanced civil transport aircraft is the efficient integration of engines on a wing in high and low speed configuration.[1] The tendency to increase the bypass ratio of turbofan engines from approximately 6 up to 10 since the last decade, which was mainly driven by the objective to reduce the specific fuel consumption and engine noise, can result in a lift loss and an increasing installation drag. This is directly related to the engine size and their locations as it has been investigated in several European projects (DUPRIN, ENIFAIR, AIRDATA).[2–7] Although aerodynamic effects are not the only important aspects during engine integration,[8] this work is focused on numerical and aerodynamic questions.

Since 1990 successive investigations in the field of engine–airframe integration have been performed by different researchers.[8–14] At DLR the F6 (high speed, through–flow nacelles, see figure 1) and ALVAST (low and high speed with turbo–powered simulators) configurations, which are similar to an Airbus–type aircraft, have been extensively used for analysis. The work for F6 included wind tunnel campaigns in cooperation with ONERA and numerical computations using Euler and Navier–Stokes techniques for different engine types and positions.[6, 7, 9, 15–18]

Fig. 1 DLR–F6 with VHBR nacelles in ONERA S2MA wind tunnel

Although in the early 90s first steps towards unstructured CFD techniques have been undertaken also at DLR[19] the numerical investigations have been concentrated on the multiblock structured grid approach during the last years for reasons of numerical accuracy. It had been demonstrated that Euler and simplified Navier–Stokes solutions can be used to predict and understand the main interference effects and flow features (e.g. lift loss, shock movement). But the advantages of numerical studies, e.g. decomposition of lift and drag for the aircraft components could not be fully utilized because Navier–Stokes results with high accuracy and verified by grid refinement studies could be obtained only with an high effort. In particular the prediction of the installation drag

$$C_{D_{install}} = C_{D_{with\,engine}} - C_{D_{clean}} - C_{D_{internal}}$$

for different engines and their positions was too time consuming.

After first Navier–Stokes results for realistic aircraft configurations became available the importance of CFD validation and verification has been stressed more by the CFD community[20–24] during the last years. In the frame of the national german project MEGAFLOW I an extensive validation and verification process has been started several years ago for structured and unstructured Navier–Stokes results using different configurations.[25] Besides extensive tests in industry, verification studies at DLR for the F6 configuration have been performed applying grid refinement, different turbulence models, and numerical parameter. It was demonstrated that even with 16 million grid points (structured) for a wing–fuselage con-

*Research Engineer, Configuration Aerodynamics Department, AIAA member.

†Graduate Student, RWTH Aachen.

figuration a variation of the drag coefficient of nearly 2.5% compared to a zero mesh element size extrapolated value can be observed depending on the grid and flow conditions.[26]

The structured grid generation for this type of configuration was a time–consuming and a labour intensive process. Between two and four month were needed for initial grids although the grid generation system MegaCads is fully parametric.[27] It was found that grids for different engines and positions, especially when closed coupled, could not be realized in a time frame demanded by industry. Due to these reasons and because for configurations with deployed high lift devices grid generation becomes even more complex,[28] it was decided to strengthen the unstructured/hybrid activities in the MEGAFLOW II project. Although the potential of unstructured techniques has been already demonstrated by other researchers,[29–31] the authors still see the necessity to verify the drag prediction capabilities of a hybrid Navier–Stokes system. This holds especially for the Tau software[32,33] in conjunction with the highly automated hybrid grid generation system Centaur.[34,35]

While in the past the DLR engine/airframe research activities have been focused on understanding basic flow features of these configurations the objective now is to compute the installation drag for conventional and Very–High–Bypass–Ratio (VHBR) nacelles for different geometric positions precisely. This becomes important when numerical optimization techniques will be applied in the future which take into account engine position, nacelle, and wing shape simultaneously. Without a reproducable accuracy, design modifications may lead to non–optimal solutions. Thus results have to be verified using grid refinement techniques and have to be compared to experiments to determine whether the installation drag values for different configurations observed in the wind tunnel can be predicted within a reasonable accuracy.

The work presented here will concentrate on installation effects at cruise conditions because a large set of experimental data from different projects is already available. Studies of installation effects with powered engines and at take–off and landing speed will be performed in other projects, e.g. EUROLIFT, AIRDATA.[6,7,28]

Configuration

The DLR–F6 configuration represents a twin engine wide body aircraft of Airbus type and is derived from the ealier F4.[36] For a design cruise Mach number of $Ma_\infty = 0.75$ the lift coefficient is $C_L = 0.5$. Figure 2 represents the geometrical data. The aspect ratio is $\Lambda = 9.5$ and the leading edge angle is $\phi = 27.1°$. The engines are represented by throughflow nacelles. Three different nacelles are available, a CFM56 like type with long and short duct, and a VHBR nacelle.

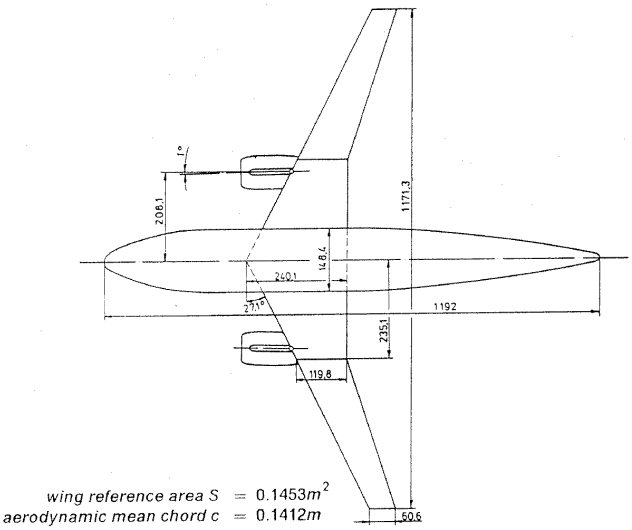

Fig. 2 DLR–F6 geometry with conventional CFM56–type nacelles

Because of ongoing work only results for the long and the VHBR nacelle will be discussed. All nacelles have an axis-symmetrical shape. The mass flow represents the real engine intake mass flow. The engine exit flow is not reproduced exactly. Due to the existence of this shortcoming in the experiments as well as in the numerical investigations verification is not affected negatively. For the conventional long nacelle three and for the VHBR nacelle two different positions have been tested in the wind tunnel. The positions are characterized by a distance in x and z direction between the wing leading edge and the nacelle upper trailing edge (x_{TE}, z_{TE}) in relation to the local wing chord length c respectively (see figure 3 and table 1).

Table 1 Nacelle locations

Nacelle	x_{TE}/c	z_{TE}/c
CFM56–long, position 1	0.49	−0.189
CFM56–long, position 2	0.30	−0.189
CFM56–long, position 3	0.30	−0.250
VHBR, position 1	−0.05	−0.120
VHBR, position 2	0.00	−0.120

Experiments

For the different configurations test campaigns have been performed in the period from 1993 to 1998 in the ONERA S2MA pressurized wind tunnel (see figure 1). The F6 model was sting mounted in the $1.77m \times 1.75m$ transonic test section. Pressure distributions are measured by 288 taps located in 8 spanwise wing sections and 47 locations in 3 radial sections of the nacelle. The Mach number was varied between $Ma_\infty = 0.6$ and 0.8 and the Reynolds number was kept constant at $Re = 3 \cdot 10^6$. During the campaign standard deviations of drag coefficients between $0.3 \ldots 0.9 \cdot 10^{-4}$ have been measured. In each test campaign wing–fuselage measurements had been included

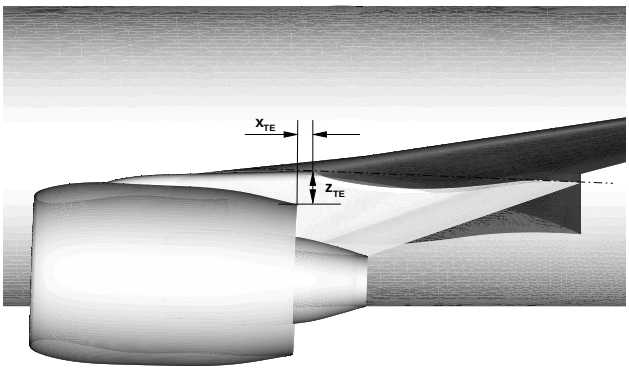

Fig. 3 Definition of nacelle position

for reference purposes. It has been observed that drag increased slightly from one campaign to another, probably due to a small deterioration of the geometry. The results presented in this work include the deviations.

Numerical Method

DLR Tau Navier–Stokes Software

For the solution of the Reynolds–averaged Navier–Stokes equation the DLR Tau software, which is still under development, is used. Tau is a finite–volume vertex–based solver with an edge–based data structure. Together with a dual–grid technique the usage of different element types, e.g. tetrahedrals, prismatic cells, pyramids, and hexahedrals is possible. The discretization of the convective fluxes has been realized with a 2nd order central difference scheme with scalar dissipation which will be used for these investigations. Roe– and AUSM type upwind schemes are also implemented. The viscous fluxes are discretized using central differences. Time integration to steady state is accomplished with a 3–stage Runge–Kutta scheme. For convergence acceleration local time stepping, residual smoothing, and multigrid is available and used here. The parallelization is based on MPI. One– and two–equation turbulence models are available. The Spalart–Allmaras model is used in these investigations.[37]

Hybrid Grid Generation

It is well known that the density and quality of grids is of great importance for solution accuracy. Therefore it is necessary to have a grid generation system that is on the one hand able to generate high quality hybrid grids and on the other hand it should to do this as much automatic as possible.
DLR uses the software package from CentaurSoft.[34,35] The system consists mainly of two parts. An interactive program which reads in CAD data in IGES format and performs some CAD cleaning if necessary. It also allows the modification of boundary conditions and element sizes if the user does not prefer the default

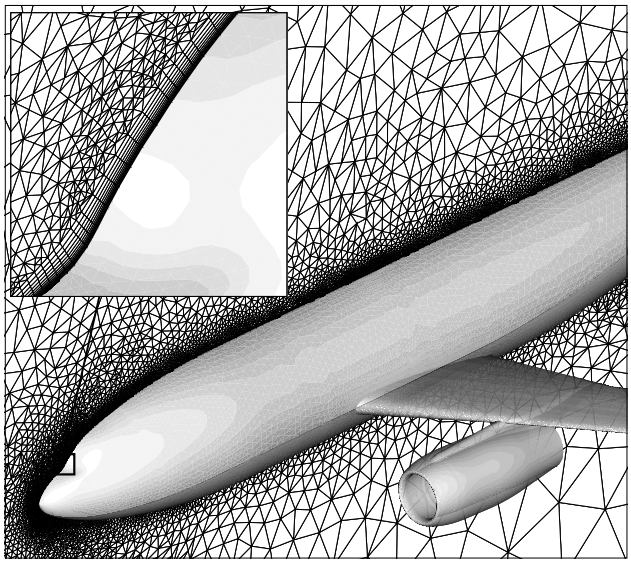

Fig. 4 DLR–F6 with conventional nacelles, adapted hybrid grid in symmetry plane

values. Different parameters control the surface, prismatic and tetrahedral element sizes. A selection of user definable sources offers the possibility to generate grids of the desired density in certain areas. In a second step the complete grid will be computed automatically.
The wing surfaces are meshed with triangles which have been stretched in spanwise direction (stretching approx. 2.5) to reduce the number of cells in directions where only small gradients of the flow are expected. Normal to the surface 24 prismatic cells with a intial stretching ratio of approximately 1.22 are generated. Figure 4 and 5 show grid cells in the symmetry plane and for a fieldcut through the VHBR nacelle. Particular attention was given to obtain a smooth transistion between the prismatic and tetrahedral elements.

In regions of CAD panel intersections or of close proximity the number of prismatic cells can be reduced automatically to maintain grid quality. The regions up to the far field are represented by tetrahedral elements. In some areas pyramids become necessary to connect faces of prismatic cells and tetrahedral elements.

The initial grid densities are 2.5 million nodes for the wing–fuselage (WB) and $\approx$ 4.6 million nodes for the configurations with nacelles. These grids can be generated in one day including the setup when the CAD geometry fulfills the requirements for a solid model. Figure 6 presents a fieldcut through the wing and the CFM56–long nacelle and displays the grid density of the inital grid.

Grid Adaptation

Solution based grid adaptation is used to refine elements. A combination of the Centaur and Tau adaption is applied using velocity and total pressure gradients because Centaur takes the original CAD data for the projection of new surface nodes into account while

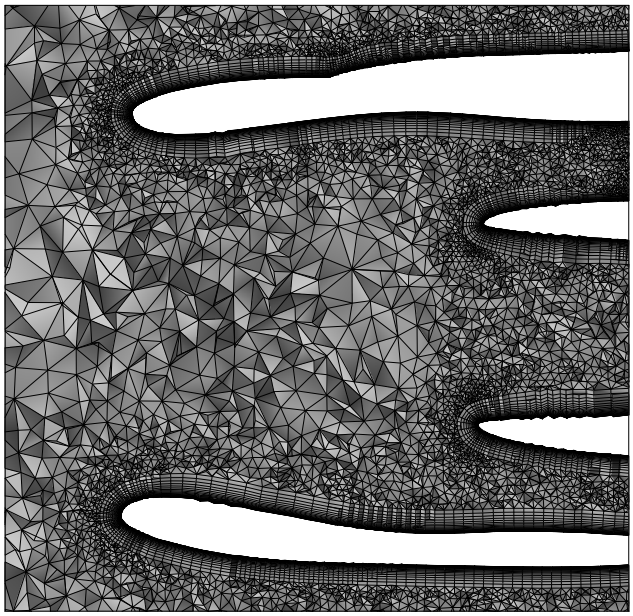

Fig. 5 Initial hybrid grid field cut through VHBR nacelle

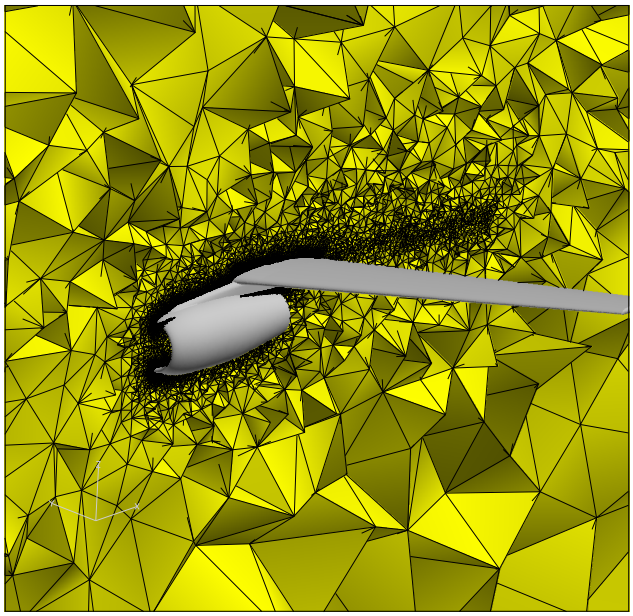

Fig. 6 Initial hybrid grid field cut through CFM56–long nacelle

Tau shows better adaptation results in the wake field and the boundary layer. A technical description of the Tau adaptation can be found in reference.[38]

Three adaptations have been performed for the wing-fuselage and the CFM56–long nacelle configurations. Only two adapations for the VHBR configuration had been possible so far due to the higher inital amount of nodes and because grid sizes should not exceed 9 million nodes to avoid too high costs. The grid densities for the various configurations are listed in table 2.

Table 2 Grid densities $[10^6 nodes]$

	WB	CFM–1	CFM–2	CFM–3
initial	2.90	4.65	4.60	4.50
1st adap	3.53	5.50	5.69	5.36
2nd adap	4.41	6.38	6.96	6.83
3rd adap	5.52	7.46	7.44	7.74

	VHBR–1	VHBR–2
initial	4.70	4.55
1st adap	6.71	6.50
2nd adap	8.46	8.19

Results

Calculations have been performed for a Mach number $Ma_\infty = 0.75$ and a range of lift coefficients of $C_L = 0.5 \ldots 0.2$ and with a fixed transistion at the same position like for the wind tunnel model. After approximately 1200 multigrid iterations on an initial grid, when the main flow features are established, the first grid adaptation has been started. The angle of attack was modified to obtain a specified target lift. The target was reached when C_D is within a tolerance of ± 0.000025 the next adaptation has been performed. Figure 7 shows a typical convergence rate of density residuals and lift and drag. The main peaks appear due to a restart with an adapted grid while the small disturbances are results of angle modifications to meet the target lift. It was of great importance that the complete parameter setting for the grid generation, Tau input, and the adaptation has been kept constant for all configurations.

Using four processors on a NEC–SX5, the computational turn–around time including three grid adaptations with node numbers up to 7.7 million averages to approximately 60h CPU time to reach a specified target lift.

CFM56 Nacelle

Polars

For verification purposes the comparison of numerical results with experimental data as well as grid refinement studies are of interest. Figure 8 displays the comparison of the computed lift polar (finest grid) for different CFM56–long nacelle positions and the wing–fuselage (WB) configuration together with the experimental data. The differences of C_L versus α for the nacelle positions can be computed. A nearly constant angle shift between the experiments and the numerical results is observable. The drag polar for the four configurations is visualized in figure 9. The results for the finest grid is compared with experiments. The standard deviation of the experiments during one campaign is equivalent to the thickness of the curves while the variation from one wind tunnel campaign to another is pictured by horizontal lines at several lift coefficients. The experiments show a variation of less

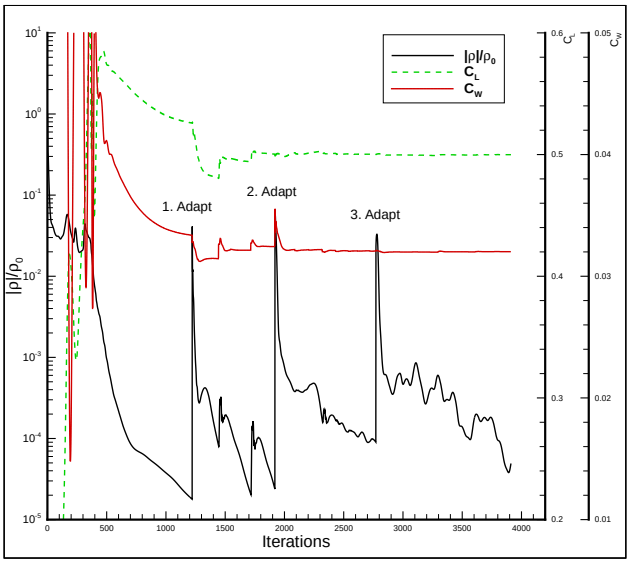

Fig. 7 Convergence of density, lift, and drag, CFM56–long, pos.1

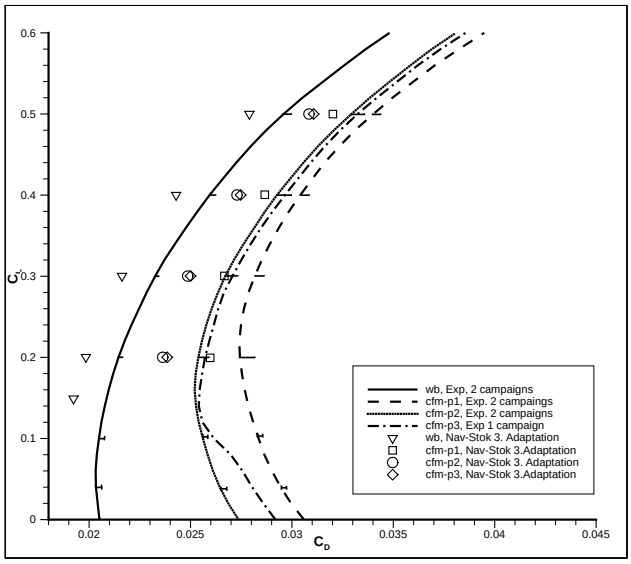

Fig. 9 CFM56–long, drag polar, numerical (finest grid) and experimental results

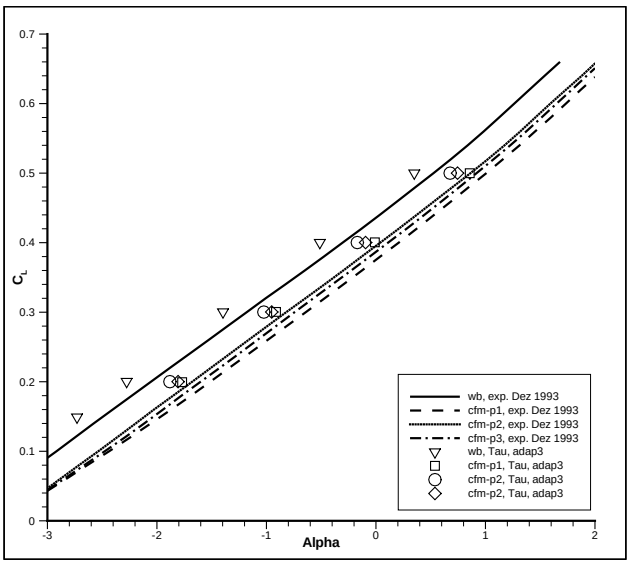

Fig. 8 Lift versus Alpha, numerical (finest grid) and experimental results

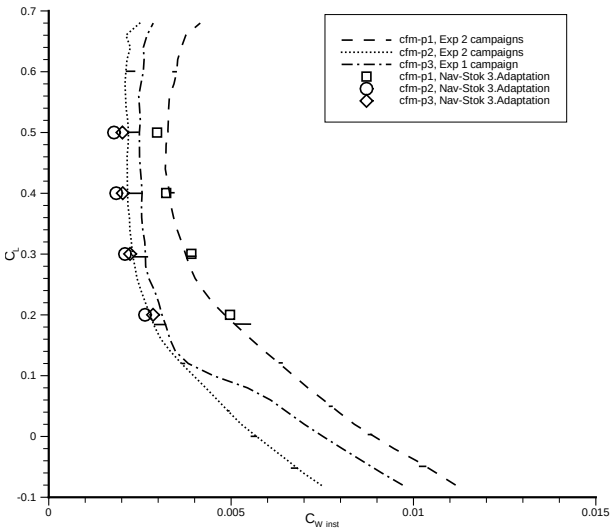

Fig. 10 Installation drag, numerical (finest grid) and experimental results

than one drag count ($dc = 10^{-4}$) during a test but up to 7 drag counts between different campaigns. The differences between the configurations due to the varying nacelle positions are not significanlty affected by this effect. It can determined that the nacelle position 2 shows the minimal total and installation drag for the computations and the experiments.

Although an offset between the calculations and the wind tunnel data of approximately 16 drag counts is visible for all configurations, the small differences due to varying engine positions can be computed within an accuracy of less than 2 drag counts for the selected lift coefficients. Based on these results and the value for $C_{D_{internal}}$ which was measured in calibrations tests ($C^{Exp}_{D_{internal}} = 11.6 \cdot 10^{-4}$) and computed ($C^{Num}_{D_{internal}} = 11.5 \cdot 10^{-4}$) the installation drag can be evaluated. Figure 10 shows that $C_{D_{install}}$ and its increase with decreasing lift is calculable. The too low drag values seen in figure 9 have been compensated partially so that the offset to the experimental data could be reduced to 1 to 4 drag counts. The deviations are approximately of the same amount as observed for different test campaigns.

Grid Refinement and Grid Convergence

The influence of the grid refinement on the overall and the installation drag is visible in figures 11 and 12. They display that an increase of the number of nodes up to approximately 7.5 million (≈24 million elements) in areas with high flow gradients effects the installation drag in a way that the difference to the experiments is reduced. The difference between the

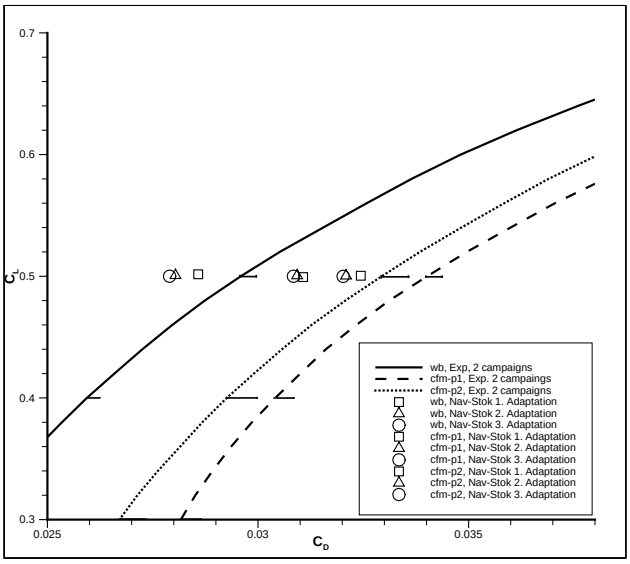

Fig. 11 CFM56–long: influence of grid density on the drag polar

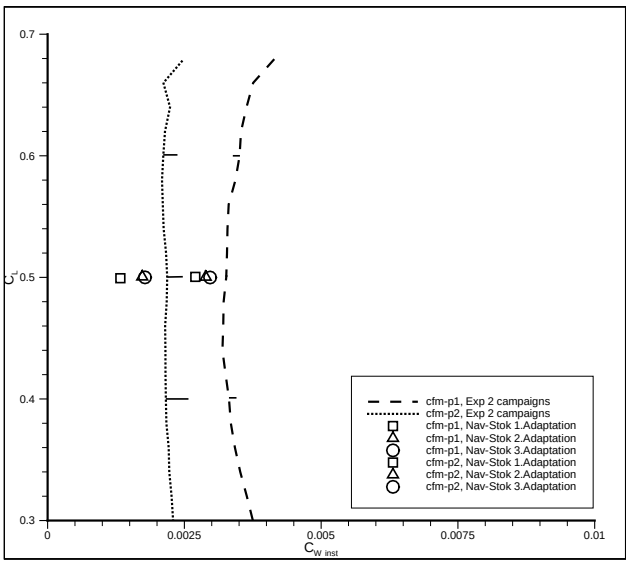

Fig. 12 CFM56–long: influence of grid density on the installation drag

2nd and 3rd adaptation is significantly smaller than between the 1st and the 2nd adaptation although more points are inserted between the 2nd and 3rd step. This is an indication that a reasonable grid density has been already chosen.

The numerical solutions depend on the number of nodes, the order of the method, and the geometrical dimension. The solution is proportional to:

$$\frac{1}{N^{2/3}}$$

for a second order accurate method in xyz–space. Different strategies for the extrapolation of solution values to infinite fine meshes can be found in the literature.[20, 22] They are based on successively refined grids, mostly of structured type. Whether these strategies

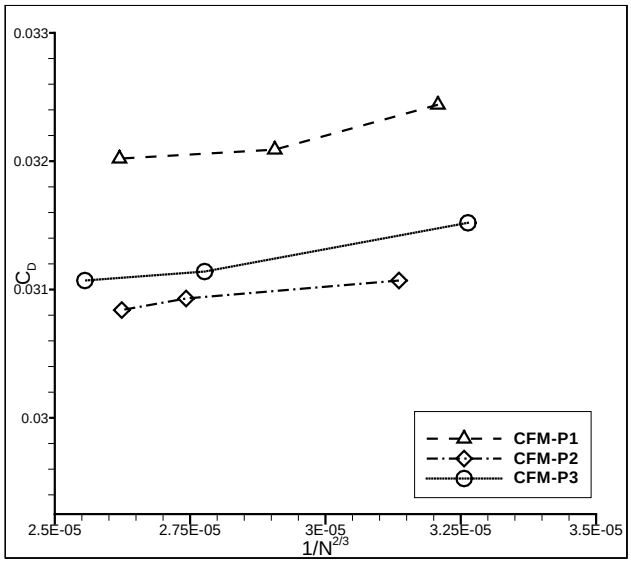

Fig. 13 CFM56–long: grid convergence

can be applied in a sensible way to unstructured grids is currently under discussion. An important prerequisite is that the adaptation adds points where high gradients and discretization errors occur. Otherwise it cannot be expected that finer grids show solutions which are suited for extrapolation techniques. The adaptation used in these investigations inserts points in the field and shifts the prismatic cells in the boundary layer, but it cannot insert new prismatic cells. Due to this fact it can be supposed, that the adaptations affect more the pressure than the viscous drag contributions.

Figure 13 presents the drag versus the number of nodes for the three CFM56–long nacelle positions. Because Tau is not at all points second order accurate the values are not found on a straight line. Applying a linear extrapolation strategy of drag for this diagram a change between 1.5% (5dc) and 2.8% (8.8dc) towards lower drag values can be computed.

Pressure distributions

The figures 14 and 15 present the pressure distribution of the CFM56–long nacelle at position 1 for a pylon inboard ($\eta = 0.331$) and outboard ($\eta = 0.377$) section. The pressure measurements from two test campaigns are plotted and indicate the possible variation of the values. For the inboard section a slightly overprediction of C_p can be found at the nose section on the upper side and on the lower wing surface where a strong flow acceleration is also visible for nacelle position 1. The deviation in the rear part on the lower side was unknown in previous structured computations.[26] Currently, investigations have been started to verify if any geometry discrepancies have been occured. The outboard section (see figure 15) shows a more acceptable result.

The aerodynamic influence of the three nacelle positions can be observed for both sections in the figures 16

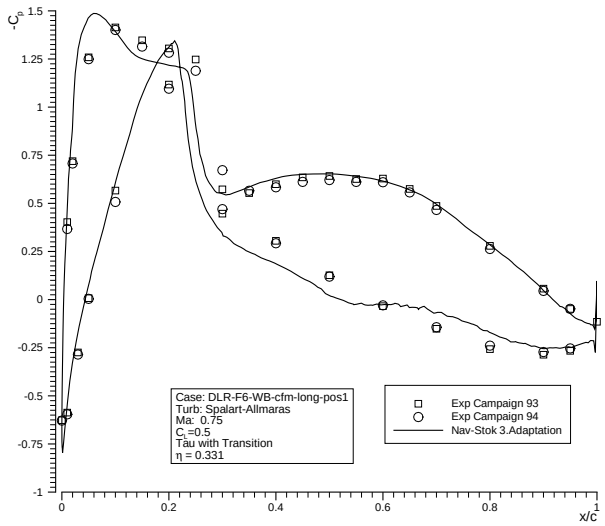

Fig. 14 CFM56–long, pos.1, pressure distribution, pylon inboard

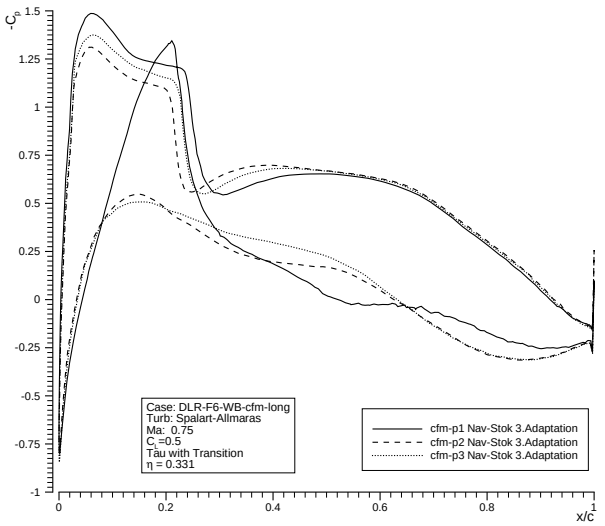

Fig. 16 CFM56–long, computed pressure distribution, pylon inboard

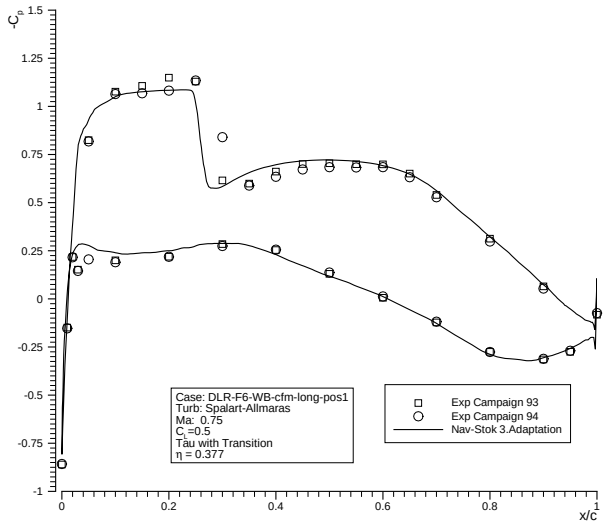

Fig. 15 CFM56–long, pos.1, pressure distribution, pylon outboard

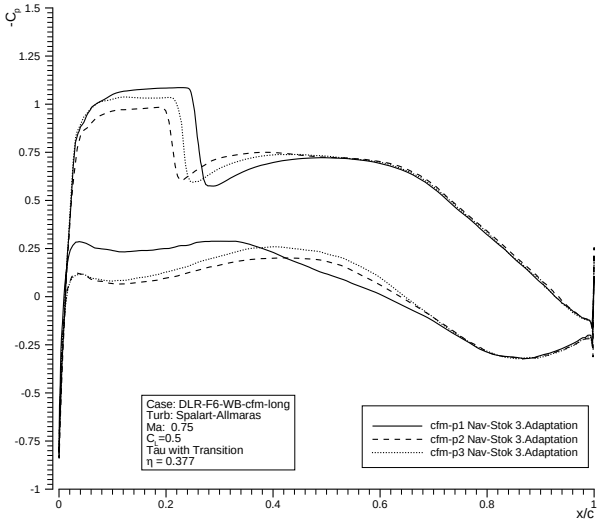

Fig. 17 CFM56–long, computed pressure distribution, pylon outboard

and 17. For comparison purposes the measured data is plotted in figures 18 and 19. Comparing the results the main effects, e.g. shock movement, flow acceleration, can be clearly computed as demonstrated already with Euler calculations.[15] As stated in previous work by researchers from ONERA and DLR[16] the study shows that the interference effects are more sensitive to a shifting of x then z.

VHBR Nacelle

The verification has been extended to include also the VHBR nacelle. In contrast to the CFM56–long nacelle the size and an additional inner part differentiate the geometries. It was the objective to maintain the same grid parameter for the initial grid and to reduce unavoidable initial differences influencing the solution by successive adaptation steps. Nevertheless the inital grid parameter needed some minor changes for the VHBR surface grids to maintain most similar prismatic cell layers.

Figure 20 and 21 presents the results of the drag polar and the installation drag. The same kind of deviations as observed for the CFM56–long nacelle are existing. The computed installation drag is based on the measured internal nacelle drag from the experiments because the computations of the internal drag for the VHBR nacelle is more expensive than for the CFM56–long nacelle. The forces on the internal geometry, beginning at the nacelle stagnation line, and part of the pylon have to be taken into account carefully in the same way as in the experiments. This work is not finished yet. Due to the observed lower

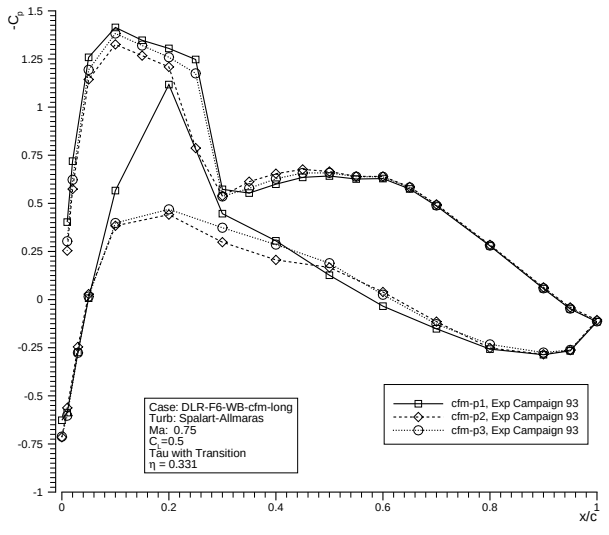

Fig. 18 CFM56–long, measured pressure distribution, pylon inboard

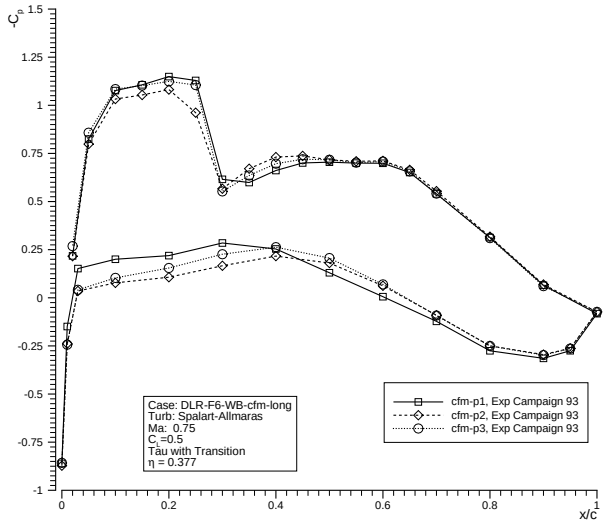

Fig. 19 CFM56–long, measured pressure distribution, pylon outboard

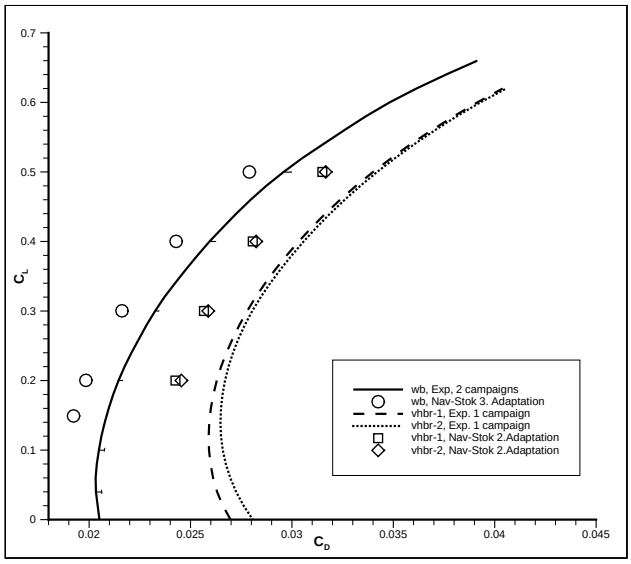

Fig. 20 VHBR, drag polar, numerical (finest grid) and experimental results

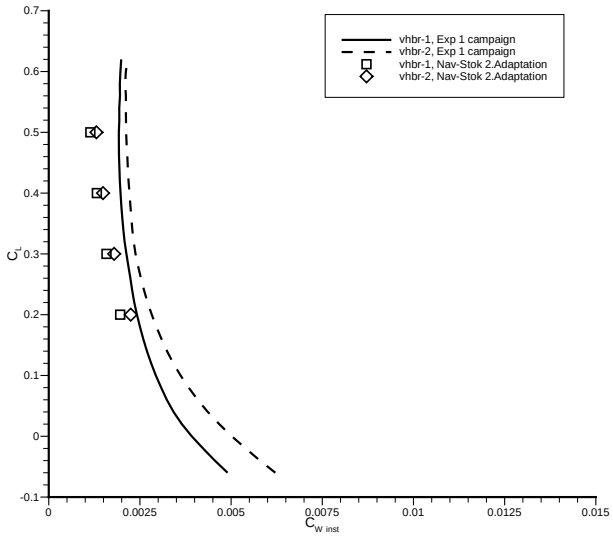

Fig. 21 VHBR, Installation drag, numerical (finest grid) and experimental results

computed drag than the experimental drag, it can be expected that also a lower internal drag for the VHBR nacelle will be calculated. That would shift the computational results of the installation drag slightly into the direction of the experiments.

Conclusion

It can be summerized that an accurate computation of installation drag during engine / airframe integration design studies (cruise flight conditions) applying hybrid Navier–Stokes methods is possible. Using consistent and constant grid generation and computational procedures, including all parameter settings, an accuracy of less than 1% regarding the installation drag in comparison with the experimental data can be achieved, although the total drag is predicted only within 6%–8%. This means that differences of 1–2 drag counts of the installation drag for varying engine locations or sizes can clearly be analyzed. Grid refinement has shown that the computed installation drag values shift towards the experiments, while the total drag is reduced. This indicates that a systematic deviation of total forces between numerical and experimental results will remain, but that the differences due to the geometries can be calculated more precisely with finer grids. The ongoing investigations will address questions of grid refinement including the prismatic layers which had to be kept constant here. The work will also focuse on new VHBR locations to possibly find a position with a similar installation drag compared to the conventional nacelle.

References

[1]Hurez, A., "Recent Progress on Powerplant / Airframe Integration at Aerospatiale Matra Airbus," *Proc. of Workshop on EU–Research on Aerodynamic Engine/Aircraft Integration for Transport Aircraft*, DLR Braunschweig, 2000, pp. 2.1–2.10.

[2]Burgsmüller, W., Hoheisel, H., and Kooi, W., "Engine/Airframe Interference on Transport Aircraft with Ducted Propfans – The European Research Program DUPRIN," ICAS Paper 94–6.2.1, 1994.

[3]Burgsmüller, W., Rollin, C., and Rossow, C.-C., "Engine Integration on Future Transport Aircraft – The European Research Programs DUPRIN/ENIFAIR," ICAS Paper 98–5.6.2, 1998.

[4]Rudnik, R. and Rossow, C.-C., "Numerical Simulation of Engine/Airframe Integration for High–Bypass Engines," *Proc. of Eccomas Conference*, Sep. 2000.

[5]Dumas, A., Godard, J., and Marin, L., "Analysis of ENIFAIR High Speed Test Results – An Evaluation of Interference Effects," *Proc. of Workshop on EU–Research on Aerodynamic Engine/Aircraft Integration for Transport Aircraft*, DLR Braunschweig, 2000, pp. 6.1–6.20.

[6]Laban, M., "Aircraft Drag and Thrust Analysis, Project Overview and Key Results," *Proc. of Workshop on EU–Research on Aerodynamic Engine/Aircraft Integration for Transport Aircraft*, DLR Braunschweig, 2000, pp. 9.1–9.15.

[7]von Geyr, H. F., "Key Results of Detailed Thrust and Drag Studies on the ALVAST Configuration," *Proc. of Workshop on EU–Research on Aerodynamic Engine/Aircraft Integration for Transport Aircraft*, DLR Braunschweig, 2000, pp. 12.1–12.17.

[8]Berry, D., "The Boeing 777 Engine/Aircraft Integration Aerodynamic Design Process," *Proc. of ICAS Congress*, ICAS,AIAA, 1994, pp. 1305–1320.

[9]Rossow, C.-C., Godard, J., Hoheisel, H., and Schmitt, V., "Investigation of Propulsion Integration Interference on a Transport Aircraft Configuration," AIAA Paper 92–3097, 1992.

[10]Rill, S. and Becker, K., "Simulation of Transonic Flow over Twin–Jet Transport Aircraft," *AIAA Journal of Aircraft Vol. 29, No. 4*, 1992, pp. 640–646.

[11]Kao, T., Su, T., and Yu, N., "Navier–Stokes Calculations for Transport Wing–Body Configurations with Nacelles and Struts," AIAA Paper 93–2945, 1993.

[12]Rossow, C.-C. and Hoheisel, H., "Numerical Study of Interference Effects of Wing–Mounted Advanced Engine Concepts," ICAS Paper 92–3097, 1992.

[13]Chaput, E., Gacherieu, C., and Tourette, L., "Application of Navier–Stokes Methods for Engine / Airframe Integration," *Proc. of DLR Workshop on Aspects of Engine–Airframe Integration for Transport Aircraft*, DLR Mitteilung 96–01, 1996, pp. 7.1–7.12.

[14]Hoheisel, H., "Aerodynamic Aspects of Engine–Aircraft Integration of Transport Aircraft," *Aerospace Science and Technology*, Nov. 1997, pp. 475–487.

[15]Rossow, C.-C., "Efficient Computation of Inviscid Flow Fields Around Complex Configurations Using a Multiblock Multigrid method," *Applied Numerical Methods, Vol. 8*, 1992, pp. 735–747.

[16]Godard, J., H.Hoheisel, Rossow, C.-C., and Schmitt, V., "Investigation of Interference Effects for Different Engine Positions on a Transport Aircraft Configuration," *Proc. of DLR Workshop on Aspects of Engine–Airframe Integration for Transport Aircraft*, DLR Mitteilung 96–01, 1996, pp. 11.1–11.22.

[17]Godard, J., Brodersen, O., and M.Hepperle, "Aerodynamic Interference Effects with Engines of different Bypass ratio on the Generic F6 transport Aircraft Configuration," *Proc. of 7th European Propulsion Forum: Aspects of Engine/Airframe Integration*, CEAS, 1999, pp. 75–84.

[18]Brodersen, O. and Rossow, C.-C., "Calculation of Interference Phenomena For a Transport Aircraft Configuration Considering Viscous Effects," *Proc. of European Forum: Recent Applications in Aeronautical CFD*, Royal Aeronautical Society, 1993, pp. 6.1–6.13.

[19]Ronzheimer, A., "Lösung der zweidimensionalen Euler–Gleichungen durch eine Finite–Volumen Diskretisierung auf unstrukturierten Netzen," *Proc. of ICAS Congress*, DLR Projektbericht, 1989.

[20]Roache, P., "Verification of Codes and Calculations," *AIAA Journal, Vol. 36, No. 5*, 1998, pp. 696–702.

[21]Rubbert, P., "On Replacing the Concept of CFD Validation with Uncertainty Management," Presentation at Daimler-Chrysler, Stuttgart, 10th June, 1998.

[22]Oskam, B. and Sloof, J., "Recent Advanves in Computational Aerodynamics at NLR," Aiaa paper 98–0138, 1998.

[23]Habashi, W., Dompierre, J., Bourgault, Y., Fortin, M., and Vallet, M.-G., "Certifiable Computational Fluid Dynamics Through Mesh Optimization," *AIAA Journal, Vol. 36, No. 5*, 1998, pp. 703–711.

[24]Jameson, A. and Martinelli, L., "Mesh Refinement and Modeling Errors in Flow Simulation," *AIAA Journal, Vol. 36, No. 5*, 1998, pp. 676–685.

[25]Kroll, N., Rossow, C.-C., Becker, K., and F.Thiele, "MEGAFLOW – A Numerical Flow Simulation System," *Proc. of 21st ICAS Conference*, ICAS, 1998.

[26]Brodersen, O., Monsen, E., Ronzheimer, A., Rudnik, R., and Rossow, C.-C., "Computation of Aerodynamic Coefficients for the DLR–F6 Configuration using MEGAFLOW," *Notes on Numerical Fluid Mechanics, Ed. W. Nitsche et.al., Vol. 72, Vieweg Braunschweig*, 1998, pp. 85–92.

[27]Brodersen, O., Hepperle, M., Ronzheimer, A., Rossow, C.-C., and Schöning, B., "The Parametric Grid Generation System MegaCads," *Proc. of 5th Intern. Conf. on Numerical Grid Generation in Computational Field Simulation.*, Ed. B. Soni et. al., 1996, pp. 353–362.

[28]Rudnik, R., Melber, S., Ronzheimer, A., and Brodersen, O., "Aspects of 3D RANS Simulations for Transport Aircraft High Lift Configurations," AIAA Paper 2000–4326, 2000.

[29]Jameson, A., Baker, T., and Weatherill, N., "Calculation of inviscid Transonic Flow over a Complete Aircraft," AIAA–Paper 86–0103, 1986.

[30]Venkatakrishnan, V., "Perspective on Unstructured Grid Flow Solvers," *AIAA Journal, Vol. 34, No. 3*, 1996, pp. 533–547.

[31]Mavripilis, D., "Parallel Performance Investigations of an Unstructured Mesh Navier–Stokes Solver," ICASE Report No. 2000–13, NASA/CR–2000–210088, 2000.

[32]Gerhold, T., Galle, M., Friedrich, O., and Evans, J., "Calculation of Complex Three–Dimensional Configurations Employing the DLR–Tau code," AIAA Paper 97–0167, 1997.

[33]Galle, M., "Ein Verfahren zur numerischen Simulation kompressibler, reibungsbehafteter Strömungen auf hybriden Netzen," Tech. rep., Dissertation, DLR Forschungsbericht 99–04, 1999.

[34]Khawaja, A. and Kallenderis, Y., "Hybrid Grid Generation for Turbomachinery and Aerospace Applications," *Intern. Journal for Numerical Methods in Engineering, No. 49*, 2000, pp. 145–166.

[35]Kallenderis, Y., "Hybrid Grids and Their Applications." *Handbook of Grid Generation, Ed. J.F. Thompson, B.K. Soni, N.P. Weatherill*, 1999, pp. 25.1–25.18.

[36]Redeker, R., Schmidt, N., and Müller, R., "Design and Experimental Verification of a Transonic Wing for a Transport Aircraft," AGARD Report CP285, 1980.

[37]Spalart, P. and Allmaras, S., "A One–Equation Turbulence Model for Aerodynamic–Flows," AIAA Paper 92–0439, 1992.

[38]Gerhold, T. and Evans, J., "Efficient Computation of 3D–Flows for Complex Configurations with the DLR–Tau Code Using Automatic Adaptation," *Notes on Numerical Fluid Mechanics, Ed. W. Nitsche et.al., Vol. 72, Vieweg Braunschweig*, 1998, pp. 178–185.